J. Fluid Mech. (2025), *vol.* 1019, A7, doi:10.1017/jfm.2025.10586

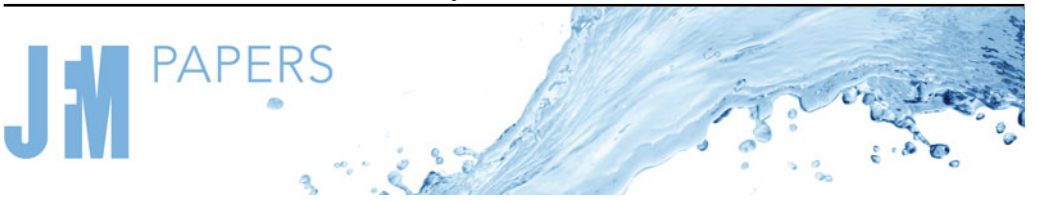

Development and interaction of Kelvin–Helmholtz vortices along two parallel fringing vegetation arrays

Yuan-Heng Zhang[1], **Alessandro Stocchino**[1] and **Huan-Feng Duan**[1]

[1]State Key Laboratory of Climate Resilience for Coastal Cities, Department of Civil and Environmental Engineering, The Hong Kong Polytechnic University, Kowloon, Hong Kong, PR China

Corresponding author: Huan-Feng Duan, hf.duan@polyu.edu.hk

(Received 26 February 2025; revised 28 July 2025; accepted 14 August 2025)

While flow confinement effects on a shear layer of an one-sided or submerged vegetation array's interface have been widely studied, turbulent interactions between shear layers in channels with vegetation on both sides remain unclear. This study presents laboratory experiments investigating flow adjustments and turbulent interaction within a symmetrical vegetation–channel–vegetation system, considering varying array widths and densities. In the outer shear layer, the shear stress is primarily balanced by the pressure gradient. As the array extends laterally, the outer penetration of the shear layer reduces from a fully developed thickness to the half-width of the open region, resulting in flow confinement. Flow confinement enhances the pressure gradient, which increases the interior velocity and shear stress at the interface. Despite the time-averaged shear stress being zero at the centreline when the shear layer is confined, the shear instabilities from both sides interact, producing significant turbulent events at the centreline with equal contributions from each side. Furthermore, the two parallel vortex streets self-organised and created a wave response with a π-radian phase shift , where alternating vortex cores amplify the pressure gradient, intensifying coherent structures and facilitating momentum exchange across the channel centreline. Although the turbulent intensity is enhanced, the decreased residence time for turbulent flow events may limit transport distance. Overall, the shear layer that develops on one interface acts as an additional resistance to shear turbulence on the other interface, leading to a more rapid decline of shear stress in the open region, despite a higher peak at the interface.

Key words: vortex interactions, shear layers, channel flow

1. Introduction

In aquatic environments, vegetation acts as an ecosystem engineer by promoting habitat diversity (Franklin *et al.* 2008), enhancing bank stability (Sukhodolov & Sukhodolova 2010) and improving water quality (Morris *et al.* 2008). Vegetation is widely distributed in various aquatic ecosystems, such as lowland rivers and their associated floodplains, coastal salt marshes with bank vegetation and estuarine channels with a boundary of mangroves. In these settings, vegetation usually occurs along river margins, partially obstructing the cross-section, which is referred to as a partly vegetated channel. The finite width of the vegetation array laterally interacts with the flow, highly altering the mean and turbulent flow structure with implications for the conveyance capacity of the channel (Mulahasan, Stoesser & McSherry 2017), and landscape evolution (Kim, Kimura & Shimizu 2015; Gurnell & Grabowski 2016).

In partially vegetated channels, many previous studies have primarily concentrated on flow adjustment (Zong & Nepf 2010) and shear-layer development (White & Nepf 2007) at the interface of the array. For instance, a diverging flow region has been observed near the leading edge of the patch, where the flow decelerates within the patch, and a part of the fluid is diverted into the open region (Zong & Nepf 2011; Liu & Nepf 2016) (figure 1). Following this flow deflection, the velocity achieves equilibrium and a shear layer with regular vortex structures forms at the interface between the patch and adjacent open region (Caroppi *et al.* 2020, 2021). These coherent vortices were triggered by a Kelvin–Helmholtz (KH) instability initiated by the strong shear and velocity inflection at the array's interface (Ghisalberti & Nepf 2002; Koken & Constantinescu 2023). Within the thickness of coherent structures, enhanced turbulent intensity and significant momentum and mass fluxes across the interface have been observed (Liu *et al.* 2008; Yan *et al.* 2022), contributing to erosion and sediment transport (Bouma *et al.* 2007; Balke *et al.* 2012). Due to the difference in hydraulic resistance in the vegetated region and in open water, the shear layer becomes asymmetric about the array's interface, forming a two-layer structure (White & Nepf 2008): (i) an inner shear layer with a penetration length of δ_I within the array and (ii) an outer shear layer with a thickness of δ_O in the open region (figure 1). In contrast to free shear layers, which can grow continuously and symmetrically downstream (Brown & Roshko 1974), the shear layer in a partially vegetated channel ceases to grow once the production of shear-layer-scale turbulent kinetic energy is balanced by its dissipation by hydraulic resistance (Ghisalberti & Nepf 2004). Consequently, when the shear layer is fully developed, the inner penetration thickness scales with the vegetation-induced drag, while the outer penetration length scales with the bed friction (White & Nepf 2007, 2008). The asymmetry effect of mixing layers is weakened as vegetation density decreases or bed friction and water shallowness enhances (Wang *et al.* 2024).

When the growth of the shear layer is constrained by the presence of a boundary before it is fully developed, the flow is referred to as a confined flow. Many previous studies have revealed that the flow confinement affects the flow adjustment (Chen, Jiang & Nepf 2013; Lei & Nepf 2021) and shear-layer evolution (Nepf & Vivoni 2000; Ghisalberti & Nepf 2009). For instance, Chen *et al.* (2013) observed a faster velocity adjustment and a higher equilibrium interior velocity, U_1, when the submergence ratio of the array (H/h, where H is the vegetation height and h is the water depth) is over a threshold value. Specifically, for a fixed canopy density (e.g. vegetation frontal area per volume, $a = 4.4\,\mathrm{m}^{-1}$), the flow adjustment length remains constant for $H/h < 0.5$, but mitigates with decreasing water level for $H/h > 0.5$. In addition, Nepf & Vivoni (2000) and Wilson *et al.* (2003) suggested that the penetration length of coherent structures into the canopy, is constrained by the water surface if $H/h > 0.5$. However, the threshold value, $H/h > 0.67$, was larger in the study of Nezu & Sanjou (2008), indicating some dependence on canopy

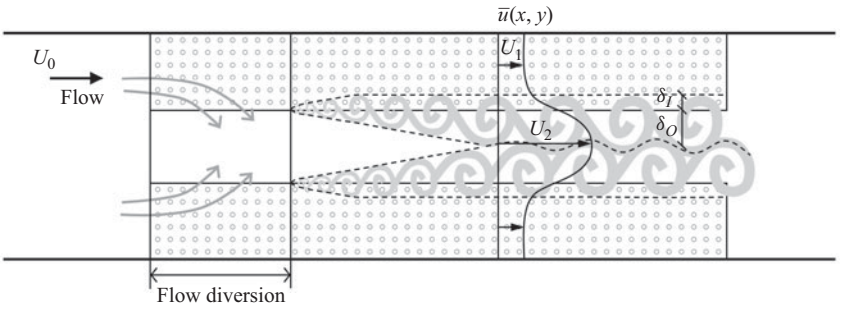

Figure 1. Conceptual diagram of flow structure in a symmetrical vegetation–channel–vegetation system. Near the leading edge of the vegetation patch, the flow is laterally diverted out of the array over an adjustment length. Shear layers form along each flow-parallel interface, producing vortices by KH instability. Here, U_1 and U_2 are the equilibrium velocities after flow adjustment within the vegetated zone and in the open region, respectively, and δ_I and δ_O denote the inner and outer penetrations of the shear layer within and outside the vegetation array, respectively.

density. Similarly, Ghisalberti & Nepf (2009) observed that the water surface constrains the growth of shear layer when $C_D a(h - H) < 0.5$, C_D is the drag coefficient of the vegetation. When the growth of shear layer was restricted by the water surface, the shear layer stopped growing (Okamoto & Nezu 2013), leading to a reduced shear-layer thickness. When the array is sparse or when the vegetation height is low, specifically when $0.1 \leqslant C_D a H < 0.23$, the inner shear layer can penetrate the entire array height, so that the penetration would be restricted by the bed (Luhar, Rominger & Nepf 2008; Zhang *et al.* 2020). This penetration highly enhances near-bed turbulence, resulting in increased sediment erosion (Zhao & Nepf 2021). Although the submergence ratio can modify the shear structure and the associated vortex size, the frequency of the KH vortex is observed to always be self-organised (Ghisalberti & Nepf 2002) and consistent with

$$f_{KH} = 0.032 \left(\frac{U_c}{\theta} \right); \tag{1.1}$$

(Ho & Huerre 1984), where $U_c = (U_1 + U_2)/2$ and θ is defined by

$$\theta = \int_{-\infty}^{+\infty} \left[1/4 - ((U(z) - U_c)/\Delta U)^2 \right] \mathrm{d}z, \tag{1.2}$$

and

$$\Delta U = U_2 - U_1. \tag{1.3}$$

Here, U_1 and U_2 are the equilibrium velocity within the vegetated zone and in the open region after flow adjustment, respectively. In a partially distributed submerged array, the lateral expansion suppresses the growth of horizontal coherent structures, weakening the horizontal shear stress (Ben Meftah & Mossa 2016). As a result, vertical coherent structures become dominant, leading to an improved inner penetration (Song *et al.* 2024). For a partially obstructed emergent array, when the array-to-channel width ratio $b/B > 0.5$, where b is the width of the array and B is the flume width, the boundary effects induced by the sidewalls become significant, allowing the along-canopy vortices to trigger the formation of along-wall vortices that rotate in the opposite direction to the original vortices (Jia *et al.* 2022). This paired-vortices pattern has been observed on two-dimensional flow past a confined circular cylinder with a blockage ratio D/B greater than 0.5, where D is the diameter of the cylinder (Sahin & Owens 2004; Wang *et al.* 2021).

Meanwhile, the initiation of the paired vortices enhances the shear-scale turbulence (Jia *et al.* 2022), and the lateral distribution of the streamwise velocity profile will shift from a hyperbolic tangent to a parabolic velocity profile (Huai, Xue & Qian 2015). These paired vortices propagate in an alternating pattern, with pronounced reduced wavelength and increased wavenumber (Jia *et al.* 2022). Moreover, the formation of along-wall vortices exerts additional resistance on the main channel flow, highly reducing the bed shear stress, which may facilitate sediment deposition (Jia *et al.* 2022).

A few previous studies have considered the evolution and interaction between two parallel shear layers. For an in-stream elongated patch, shear layers can develop at two flow-parallel interfaces simultaneously. For a low-flow blockage patch ($C_D ab < 2$, where b is the half-width of the patch), the inner penetration length is over the patch centreline, $\delta_I > b$, (Rominger & Nepf 2011), allowing shear-layer vortices to interact and merge into a von Kármán-like vortex street (Hosseini, Griffith & Leontini 2020). This vortex interaction results in a significant velocity recovery and turbulence enhancement within the patch. For a high-flow blockage patch ($C_D ab \geqslant 2$), although shear layers fully develop with a penetration length less than half the patch width, $\delta_I < b$, they can still communicate across the patch width, which highly enhances the strength of the vortices through a wave response (Zong & Nepf 2011; Rominger & Nepf 2011). The wave response refers to an oscillating wave motion within the array generated by the passage of vortex, whose centre is a low-pressure point (White & Nepf 2007). In contrast to the in-stream vegetation patch with a slow-moving flow within the patch, a symmetrical straight compound channel creates a reverse flow pattern, with a fast-moving flow in the central main channel and a slow-moving flow in the floodplain regions (Proust *et al.* 2013; Dupuis *et al.* 2017; Rathod, Timbadiya & Barman 2025). This flow distribution causes the shear layers formed at the transition regions and associated vortices to rotate oppositely. In a narrow symmetrical compound channel, the shear layer can penetrate to the channel centreline and meet the opposite shear layer, leading to a lateral confinement on shear-layer growth (Stocchino & Brocchini 2010; Peltier 2011; Stocchino *et al.* 2011). However, the interaction of shear-layer vortices in the high-discharge main channel remains insufficiently investigated, especially when two opposite shear layers meet at the channel centreline.

Previous studies have investigated the impacts of flow confinement on velocity adjustment and turbulent structures in scenarios where the vegetation is distributed on one side or submerged. However, the scenario where the vegetation is distributed on both sides of the channel has been rarely addressed, especially when the outer shear layer from one array interacts with the shear layer from the opposite array at a high blockage ratio. The inadequate research inevitably hinders the full understanding of the mechanics and interactions between a vegetation patch and water flow, such as the velocity distribution and turbulent structure, making it difficult to predict the sediment transport and morphological evolution for such scenarios that commonly exist in nature aquatic environments. In addition to its eco-hydraulic perspective, this scenario also offers fundamental insights into the mechanics of the interactions between reverse-rotating vortex streets. In this work, we consider a vegetation–channel–vegetation system to investigate the flow structure in a channel with fringing vegetation at both sides (figure 1). This symmetrical configuration creates a high-discharge flow in the central open region and a low-discharge flows in the side vegetated zones, resulting in a slow–fast–slow velocity pattern that is the reverse of that observed in an in-stream vegetation patch. Correspondingly, the shear layers developed at the lateral interfaces and associated vortices might rotate reversely, similar to the behaviour observed in a symmetrical compound channel. The flow confinement and turbulent interaction can be explored by varying patch widths and densities. Therefore, the main objectives of this study are (i) to investigate the

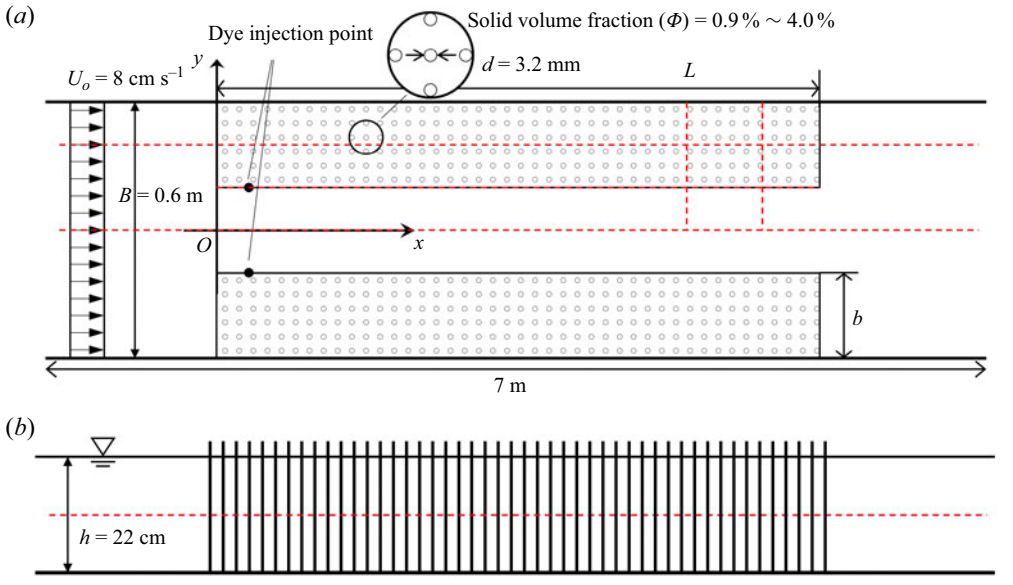

Figure 2. The experiment set-up. (*a*) Top view: illustration of the coordinate system, model array and dye injection points, longitudinal and lateral transects (red dashed lines) of velocity measurements by ADV. (*b*) Front view: velocity measurements were conducted at the middle of water depth.

flow adjustment and shear structure under a symmetrically distributed vegetated channel through scaling analysis; (ii) to examine the initiation and evolution of shear-layer vortices under varying patch widths and densities; (iii) to evaluate turbulent interaction between two parallel shear layers.

This paper is organised as follows. Section 2 details the materials, experimental set-up, data collection and processing methods, as well as the parameter definitions used in this study. Section 3 presents the main results, focusing on the flow adjustment, shear structure scaling and the initiation and development of coherent structures. Section 4 provides a detailed discussion on the interaction between two parallel shear layers, including the formation of wave motion, the behaviour of turbulent events and momentum transport. Finally, § 5 summarises the key findings and discusses the limitations and potential directions for future research.

2. Materials and methods

Experiments were carried out in a 0.6 m wide (B), 7 m long laboratory flume with a slope of $S = 0.1\,\%$. Two steel mesh screens were installed at the upstream inlet of the flume to minimise water surface oscillations. To better understand the patch-scale turbulent interaction, complex natural aquatic vegetation was simulated by simplified geometric analogues. Two symmetrical arrays of model vegetation were created by placing polyvinyl chloride (PVC) rods with a diameter, $d = 3.2$ mm, in a false bottom of perforated PVC baseboards (figure 2). The width of each array, b, was varied between 10 and 20 cm, leading to an array-to-channel blocking ratio, $2b/B = 1/3 \sim 2/3$. The leading edge of the arrays was placed in the position where the flow was laterally uniform, as confirmed by preliminary velocity measurements. The time-averaged streamwise velocity, measured at distances of 25, 45 and 65 cm upstream of the patch, yielded an average velocity of $U_o = 8\ \mathrm{cm\,s^{-1}}$, with a deviation less than 5 %. Each array has a length of $L = 3.7$ m,

Φ	dx(cm)	dy(cm)	b(m)	U_1(m s^{-1})	U_2(m s^{-1})	u_*(m s^{-1})
0.9 %	3	3	0.11	0.028 (0.001)	0.130 (0.001)	0.013 (0.005)
			0.14	0.033 (0.001)	0.141 (0.001)	0.015 (0.006)
			0.17	0.039 (0.001)	0.149 (0.001)	0.018 (0.008)
			0.20	0.046 (0.001)	0.151 (0.001)	0.021 (0.008)
1.3 %	2	3	0.10	0.024 (0.001)	0.131 (0.001)	0.013 (0.004)
			0.12	0.022 (0.001)	0.141 (0.001)	0.017 (0.007)
			0.14	0.025 (0.001)	0.151 (0.001)	0.017 (0.007)
			0.16	0.029 (0.001)	0.160 (0.001)	0.019 (0.006)
			0.18	0.034 (0.001)	0.166 (0.001)	0.021 (0.007)
			0.20	0.044 (0.001)	0.173 (0.001)	0.023 (0.007)
2.0 %	2	2	0.10	0.019 (0.001)	0.135 (0.001)	0.015 (0.006)
			0.12	0.018 (0.001)	0.147 (0.001)	0.017 (0.004)
			0.14	0.023 (0.001)	0.159 (0.001)	0.020 (0.007)
			0.16	0.027 (0.001)	0.171 (0.001)	0.021 (0.006)
			0.18	0.033 (0.001)	0.173 (0.002)	0.024 (0.007)
			0.20	0.039 (0.001)	0.183 (0.001)	0.027 (0.009)
4.0 %	1	2	0.10	0.013 (0.001)	0.141 (0.001)	0.015 (0.007)
			0.12	0.014 (0.001)	0.154 (0.001)	0.018 (0.008)
			0.14	0.019 (0.001)	0.171 (0.001)	0.021 (0.006)

Table 1. Experimental parameters and measured data. Here, dx and dy are the stem's centre-to-centre spacing in the streamwise and spanwise directions, respectively, U_1 and U_2 represent the equilibrium velocities after flow adjustment within the vegetated zone and in the open region, respectively, and u_* is the friction velocity at the side edge of the patch, defined in (3.3). Number in the bracket indicates uncertainty.

to ensure the full velocity adjustment and shear-layer development. The origin of the coordinate system ($x = 0,\ y = 0$) was located at the leading edge of the array and at the midpoint of both the open region and the flume, with the x-axis oriented in the streamwise direction (figure 2a). The velocity components in the x and y directions were denoted by u and v, respectively. As a first step for future experiments in random arrangements, the cylinders were arranged in a regular pattern. To obtain different array densities, the stem's centre-to-centre spacing was varied from dx = 1 to 3 cm and dy = 2 to 3 cm in the streamwise and spanwise directions, respectively (table 1). The array density is characterised by the frontal area per unit volume $a = Nd$, where N(m^{-2}) is the number of rods per unit bed area, ranging from 3.6 to 16.0 m^{-1}, and average solid volume fraction $\Phi = N\pi d^2/4 = 0.9\,\% \sim 4.0\,\%$. The corresponding non-dimensional flow blockage of the array was $C_Dab = 1.85 \sim 13.61$, where C_D is the is the drag coefficient of the array cylinders. Here, C_D was estimated by, $C_D = 1 + 10Re_{U_1}^{-2/3}$ (White & Majdalani 2006), where U_1 is the equilibrium velocity after flow adjustment within the vegetated region. The value of C_Dab for all cases considered is over the threshold value (table 1), $C_Dab \geqslant 0.1$, for the KH vortex initiation in a partly obstructed channel with an emergent vegetation patch (Ghisalberti & Nepf 2002; Nepf *et al.* 2007). The cylinders filled the full water depth (h), piercing the water surface, i.e. $H > h$, in which H is the height of the stem. Flow was provided by a recirculating pump. The flow depth was controlled to be $h = 22 \pm 0.2$ cm for all scenarios by an adjustable tailgate at the end of the flume. Water depth was measured with a point gauge upstream of the array. The channel Froude number and channel Reynolds number were $Fr_h = U_o/(gh)^{1/2} = 0.05$, where g (m s^{-2}) is the gravitational acceleration, and $Re_h = U_o h/\nu = 17\,600$, where $\nu(= 10^{-6}$ m^2 s$^{-1})$ is the kinematic viscosity of the water, respectively, indicating that the flow was sub-critical and turbulent. Experimental configurations are summarised in table 1.

A down-looking three-dimensional Nortek Vectrino Profiler (acoustic Doppler velocimeter, ADV) was used to collect the velocities, with a collection time of 120 s and a sampling rate of 75 Hz. Convergence tests of mean and turbulent flow statistics were conducted to ensure that the sampling duration was sufficient to avoid deviations due to inadequate collection time. The ADV is capable of collecting velocity measurements within a range of 40–72 mm from the down-looking probe, with user-defined cell sizes varying from 1 to 4 mm. In this experiment, 11 cells were selected, each with a 2 mm cell size, resulting in a total measurement length of 22 mm (i.e. 40–62 mm from the probe). This configuration was chosen to ensure high-quality sampling data. Given that the flow structure generated by an emergent patch is primarily horizontal (Zong & Nepf 2012), velocity measurements were taken only at the middle of the water depth and only horizontal components were used to represent the two-dimensional flow structure induced by emergent rods (figure 2*b*). Within the array, velocities were measured in the middle between the cylinders to reduce disturbance and heterogeneity. Measurements were taken along the channel centreline ($y = 0$) and the array centreline ($y = (B - b)/2$) to investigate the flow adjustment. Due to the symmetrical configuration and laterally uniform incoming flow, the flow structure was considered symmetrical. Velocities along the channel centreline can also reveal the interaction between the two shear structures formed at the parallel array lateral interfaces. To identify the initiation and evolution of the large-scale coherent structures, velocities were collected along one array lateral edge ($y = B/2 - b$). Lateral measurements were only conducted in one half from the sidewall to the channel centreline ($y = 0 \sim 0.8B/2$) of the flume to characterise the velocity distribution and turbulence structure. Velocity measurement near the flume wall from $y = 0.8B/2$ to $B/2$ was constraint by the ADV holder. At $y = 0.8B/2$, no sidewall effect was observed for all scenarios investigated. Lateral measurements were performed at $x = 2.5$ and $x = 3.0$ m, where the flow was verified to be fully developed in all scenarios based on the longitudinal velocity profiles and the consistency between the two transects. To avoid redundancy, only data at $x = 2.5$ m were included in the subsequent analysis. Velocity measurements were taken every 1 and 10 cm in spanwise and streamwise profiles, respectively. The transects of velocity measurements are denoted by the red dashed lines in figure 2. The equilibrium velocity within vegetated zone (U_1) and in the open region (U_2), as well as the friction velocity (u_*) at the side interface of the array (defined in (3.3)), were determined by the mean values of data collected in the fully developed region, with their uncertainties estimated by the corresponding standard deviations (table 1).

For velocity and turbulence analysis, raw ADV data with a correlation coefficient of less than 70 % were prefiltered. The spikes from ADV measurements were removed by the method of Goring & Nikora (2002), which is widely applied in vegetated flows (Liu & Nepf 2016; Zhao & Nepf 2021). Each velocity record was decomposed into time-averaged components ($\overline{u}$, $\overline{v}$) and fluctuating components (u', v'). To qualify the turbulent characteristics, the root mean square of the fluctuating velocity, $u_{rms} = \sqrt{\overline{u'^2}}$ and $v_{rms} = \sqrt{\overline{v'^2}}$ and time-averaged Reynolds shear stress, $-\overline{u'v'}$, were evaluated. The initiation and interaction of the turbulent structures were analysed using the cross-power spectral density of the streamwise and lateral velocity (S_{uv}). Here, S_{uv} was calculated by Welch's method (Welch 1967) with a Hamming window of equal size of 40 s and a 50 % overlap. The time-averaged lateral velocities ($\overline{v}$) collected at upstream region, fully developed region inside and around the array were all below 1 cm s^{-1}, indicating that no significant secondary flow occurred in the present experiment.

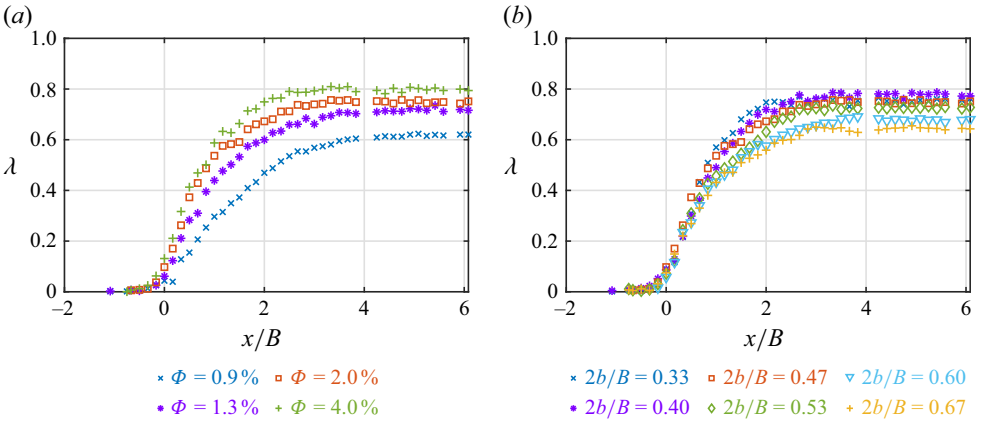

Figure 3. Velocity adjustment evaluated by the longitudinal profiles of the velocity shear across the lateral interface, $\lambda = (U_2 - U_1)/(U_2 + U_1)$, under (*a*) varying array densities for $2b/B = 0.47$, and (*b*) varying blockage ratios for $\Phi = 2.0\,\%$.

Flow visualisations were conducted to describe the flow structure, supporting the velocity measurements. Red dye and green dye were simultaneously injected at 10 cm downstream from two corners of the leading edge ($x = 10$ cm, $y = \pm(B/2 - b)$) to avoid the strong diverting effect around the leading edge on dye transport. A high-resolution camera (Sony FDR-AXP55, 3480 × 2160 pixels) was placed around 5 m above the flume to cover the test section. Yellow-coloured grid lines with a 10 cm spacing regarding both streamwise and cross-stream directions at the flume bottom were used to provide a distance reference. Several light-emitting diodes were positioned above the flume to illuminate the test section, which can avoid water surface light reflections. Videos with 25 frames per second were recorded from the beginning of the dye injection until several vortex formations were caught. Pictures were post-processed using Photoshop software to enhance the colour of the dye. To ensure water clarity for dye visualisation, water in the tank was replaced after each two experimental runs.

3. Results

3.1. *Flow adjustment and shear layer*

Flow adjustment initiated upstream of the leading edge of the arrays ($x < 0$) and continued after entering the arrays, varying with array density (Φ) and array-to-channel blockage ratio ($2b/B$). Fluids were deflected from the high-resistance vegetated regions to the low-resistance open region, leading to a mitigated velocity interior the vegetated regions (U_1) and enhanced velocity in the free-stream region (U_2). Then, the velocity shear, $\lambda = (U_2 - U_1)/(U_2 + U_1)$, across the lateral interface of the array enhanced. As the flow developed downstream, the growth rate of the velocity shear decelerated and eventually reached equilibrium. The developing region is defined as the zone between the leading edge of the patch ($x = 0$) to the position where the velocity shear achieves a constant value ($\partial\lambda/\partial x \approx 0$). Then, the region behind the developing region is defined as a fully developed region. Figure 3(*a*) observes that increasing the array density (Φ) accelerated the flow adjustment by creating a stronger flow deflection, leading to an improved velocity shear across the interface, as indicated by a larger $\partial\lambda/\partial x$ and a higher λ. As the array width varied (figure 3*b*), the overlap of λ near the leading edge of the array at different array widths revealed that the lateral flow diversion was independent of the array width. The flow

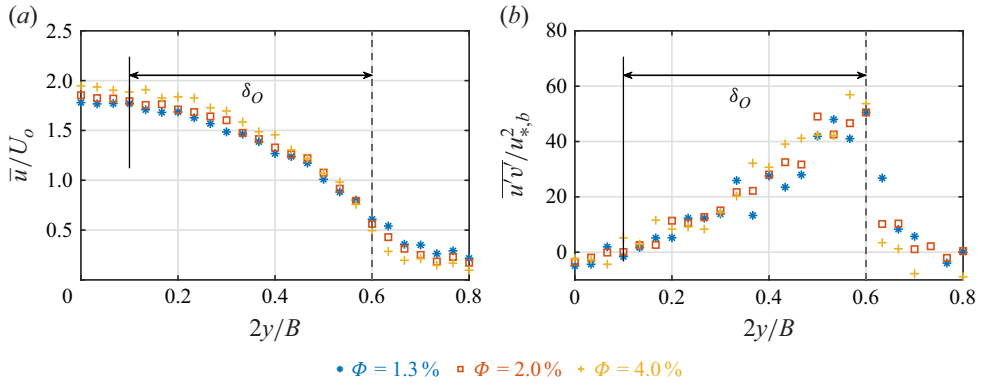

Figure 4. The influence of array density (Φ) on the (a) velocity redistribution ($\overline{u}/U_o$) and (b) normalised shear stress ($-\overline{u'v'}/u_{*,b}^2$). Data were collected in the fully developed region for cases with $2b/B = 0.40$. The dashed line indicates the lateral interface of the array. Here, $u_{*,b}$ is the bed friction velocity.

adjustment was almost identical at $2b/B < 0.5$, suggesting that the flow adjustment was not influenced. As $2b/B$ further increased, the velocity shear reduced, indicating that the flow confinement presented at $2b/B > 0.5$. The influence of the array-to-channel blockage ratio on the flow adjustment is consistent with the findings in a submerged canopy, where a higher submergence ratio (H/h) produced a weaker velocity shear at the top interface (Chen *et al.* 2013).

The shear flow near the side edge of each array exhibited a distinct two-layer structure, characterised by a rapidly varying inner penetration, δ_I, into the vegetated region and a more gradual outer penetration, δ_O, in the open region (figure 4). Within the shear layer, the shear stress was greatly enhanced, with a peak presenting at the lateral interface. The penetration length is defined as the distance from the side edge of the array to the position where the velocity becomes constant ($\partial\overline{u}/\partial y \approx 0$) and the shear stress approaches zero ($-\overline{u'v'} \approx 0$). A denser array produced a lower interior velocity (U_1) and a higher free-stream velocity (U_2), thereby enhancing the velocity shear (figures 4*a*, 3*a*). For arrays with a blockage ratio of $2b/B = 0.40$, whose lateral edge was located at $2y/B = 0.60$, it was observed that the velocity became constant and the shear stress reduced to zero at $2y/B = 0.10$, yielding an outer penetration length of $0.5(B/2)$ (figure 4). The outer penetration thickness, $\delta_O = 0.5(B/2)$, remained constant for a given array width (figure 4), independent on the array density. This observation is consistent with the findings of White & Nepf (2008), who studied a partially obstructed emergent vegetation array with a blockage ratio of $b/B = 0.33$ and reported that the outer-layer width was governed by the water depth and bed friction coefficient, both of which were held constant in the present experiment.

As the array extended laterally, the outer penetration of the shear layer reduced from the constant thickness, $\delta_O = 0.5(B/2)$ at $2b/B < 0.5$, to the half-width of the open region, $\delta_O = B/2 - b$ at $2b/B > 0.5$ (figure 5). Specially, at $2b/B < 0.5$, the streamwise velocity increased and stabilised before reaching the channel centreline (figure 5*a*), revealing that the outer layer was fully grown in the open region. The thickness of the outer shear was less than the half-width of the open region ($\delta_O = 0.5(B/2) < B/2 - b$). Within the outer shear layer, the shear stress dropped from the peak value at the interface to zero as the velocity became stable (figure 5*b*). At $2b/B > 0.5$, the streamwise velocity continuously increased in the open region, presenting a peak value at the channel centreline (figure 5*a*). In this regime, the mitigation of the interior velocity diminished, resulting in a higher U_1 and

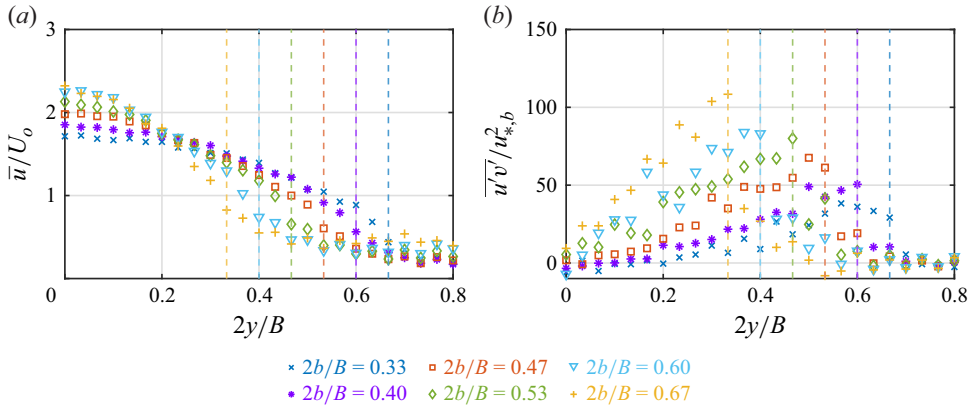

Figure 5. The lateral profiles of the (*a*) normalised time-averaged streamwise velocity ($\overline{u}/U_o$), and (*b*) normalised shear stress ($-\overline{u'v'}/u_{*,b}^2$), under varying blockage ratios ($2b/B$). Data were collected in the fully developed region for cases with $\Phi = 2.0\,\%$. The dashed lines (with corresponding colour of the case) indicate the lateral interfaces of the arrays. Here, $u_{*,b}$ is the bed friction velocity.

consequently a reduced velocity shear λ (figure 3*b*). Despite the decrease in velocity shear, the peak shear stress at the interface was highly enhanced (figure 5*b*). The shear stress decayed continuously in the open region and approached zero at the channel centreline (figure 5*b*). Consequently, the array with a higher $2b/B$ experienced a faster shear decay in the open region, as indicated by a larger $-\partial\overline{u'v'}/\partial y$. The lateral profile of the streamwise velocity and shear stress shows that the thickness of the outer layer was restricted to the half-width of the open region, $\delta_O = B/2 - b$, which was less than the full penetration length, $0.5(B/2)$ in the present work. Given the symmetrical configuration of the system, the shear layers that developed along the two flow-parallel interfaces of the arrays can simultaneously extend toward the centreline, where they may meet and interact (figure 5*b*). Increasing the width of the open region or removing the opposite array would allow the outer shear layer to continue to expand laterally. Consequently, it is considered that the development of shear layer from one array will be confined by the shear layer developed at the opposite array when they meet at the channel centreline, which will be further analysed in the following.

In partly vegetated flows, the momentum exchange between the open region and the vegetated region can be analysed by referring to the time-averaged, spatially averaged and depth-averaged two-dimensional shallow water equations (Truong, Uijttewaal & Stive 2019; Caroppi *et al.* 2021). In the fully developed region, the lateral flow diversion ceased, leading to $\overline{v} = 0$, $\partial\overline{u}/\partial x = 0$ and $\partial/\partial t = 0$. The resulting streamwise momentum equation becomes

$$0 = -\frac{1}{\rho}\frac{\partial\overline{p}}{\partial x} - \frac{\partial\overline{u'v'}}{\partial y} - F_x, \tag{3.1}$$

where ρ is the water mass density, and F_x is the drag force exerted on the fluid in the streamwise direction

$$F_x = \begin{cases} \dfrac{1}{2}\dfrac{C_f}{h}\overline{u}^2, & y < B/2 - b \\ \dfrac{1}{2}\dfrac{C_D a}{1-\Phi}\overline{u}^2, & y \geqslant B/2 - b. \end{cases} \tag{3.2}$$

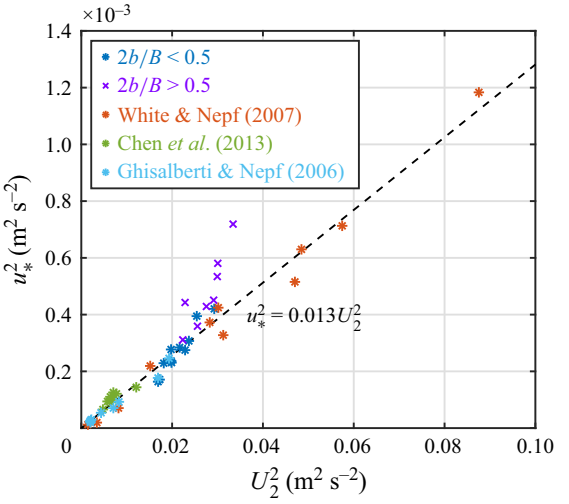

Figure 6. Interfacial shear stress, u_*^2 versus U_2^2. The dashed line is fitted from data in the unconfined condition ($2b/B < 0.5$), $u_*^2 = 0.013U_2^2$, with a $R^2 = 0.98$.

The friction velocity, u_*, was defined from the peak shear stress at the side edge of the array, τ_i,

$$u_* = \sqrt{\frac{\tau_i}{\rho}} = \sqrt{-\overline{u'v'}_{y=B/2-b}}. \tag{3.3}$$

The shear stress diminishes to zero across the shear layer. For the outer shear layer in the open region

$$-\frac{\partial \overline{u'v'}}{\partial y} = \frac{u_*^2}{\delta_O}. \tag{3.4}$$

In the outer shear layer, the shear stress approximately balances the pressure gradient. Equation (3.1) becomes

$$\frac{1}{\rho}\frac{\partial \overline{p}}{\partial x} = \frac{u_*^2}{\delta_O}. \tag{3.5}$$

For unconfined shear layer, the shear stress reduced to zero before being restricted by other confinement, leading to a zero gradient of the shear stress, $-\partial\overline{u'v'}/\partial y \approx 0$, in the region beyond the outer layer. In this region, the pressure gradient is balanced by bed friction

$$\frac{1}{\rho}\frac{\partial \overline{p}}{\partial x} = \frac{1}{2}\frac{C_f}{h}U_2^2. \tag{3.6}$$

Substituting (3.5) into (3.6) gives

$$\frac{u_*^2}{U_2^2} \sim \frac{2h}{C_f}\frac{1}{\delta_O}. \tag{3.7}$$

When the shear layers did not penetrate to the channel centreline ($2b/B < 0.50$), a constant value of u_*^2/U_2^2 was observed (figure 6), consistent with the data collected from a single along-bank vegetated channel with $b/B = 0.33$ (White & Nepf 2007). This constant ratio

confirms that the shear-scale turbulence is balanced by the dissipation by bed friction, leading to $\delta_O \sim h/C_f$ (3.7) for an unconfined shear layer. The constant ratio of u_*^2/U_2^2 was also valid in submerged rigid canopy with a submergence ratio of $h/H < 0.5$ in the experiments conducted by Ghisalberti & Nepf (2006) and Chen *et al.* (2013). However, when the shear structure penetrates to the channel centreline ($2b/B > 0.5$), the deviation of u_*^2/U_2^2 in figure 6 reveals that δ_O does not scale with h/C_f any more (3.7). As the array expanded laterally (figure 5), δ_O was restricted to half-width of the open region $B/2 - b$ and the value of u_*^2 was highly enhanced (figure 5), which resulted in an enhancement of u_*^2/δ_O. According to the balance of pressure gradient and shear stress within the outer shear layer (3.5), the pressure gradient in the open region was improved. In the unconfined condition, the pressure gradient is balanced by the bed friction. However, in the confined condition, the bed friction alone is insufficient to balance the pressure gradient. Due to the symmetrical configuration, the shear layer developed in one array contributed to balancing the shear-scale turbulence from the opposite array, performing like an extra flow resistance. In general, $\delta_O = \min[c_1 h/C_f, (B/2 - b)]$, where c_1 is the scaling factor. By fitting the measured data in the present work and data collected from previous studies (figure 6), $c_1 = 154$, with $R^2 = 0.98$. This equation suggests that flow confinement occurs at $c_1 h/C_f + b > B/2$, where $c_1 h/C_f$ in the present work is $0.5(B/2)$. This yields a threshold condition of $0.5(B/2) + b > B/2$, which simplifies to $2b/B > 0.5$ for the present experiment. However, when bed friction increases or water depth decreases, the outer shear layer exhibits a reduced full penetration length (i.e. smaller $c_1 h/C_f$). Then, the threshold value for flow confinement increases, and a higher blockage ratio is required to generate flow confinement.

Inside the array, the region beyond the inner shear layer has $-\partial\overline{u'v'}/\partial y \approx 0$. In this region, the pressure gradient was balanced by the drag resistance induced by the plants. Assuming the pressure gradient is constant in the lateral direction and applying (3.5), the streamwise momentum equation (3.1) becomes

$$\frac{1}{2}\frac{C_D a}{1-\Phi}U_1^2 = \frac{u_*^2}{\delta_O}. \tag{3.8}$$

Thus

$$\frac{u_*^2}{U_1^2} \sim C_D a \delta_O. \tag{3.9}$$

By fitting the measured data, it is obtained that $u_*^2/U_1^2 = 0.5 C_D a \delta_O$ with $R^2 = 0.83$ (figure 7*a*). This agreement suggests the pressure gradient in the open region influences the adjustment of the interior velocity ((3.5) and (3.8)). Specially, an enhanced pressure gradient due to shear-layer confinement in the open region leads to a higher interior velocity U_1, consistent with the lateral profiles of streamwise velocity shown in figure 5(*a*), where U_1 was observed to increase with $2b/B$. This interior velocity enhancement was also observed in a submerged canopy with a higher submergence ratio (Chen *et al.* 2013; Lei & Nepf 2021). The submergence ratio, defined as the ratio of vegetation height to water depth, performs similarly to a horizontal blockage ratio in the present work, but applies in the vertical direction.

According to (3.7) and (3.9), we obtain

$$\frac{U_1^2}{U_2^2} \sim \frac{h}{C_f}\frac{1}{C_D a \delta_O^2}, \tag{3.10}$$

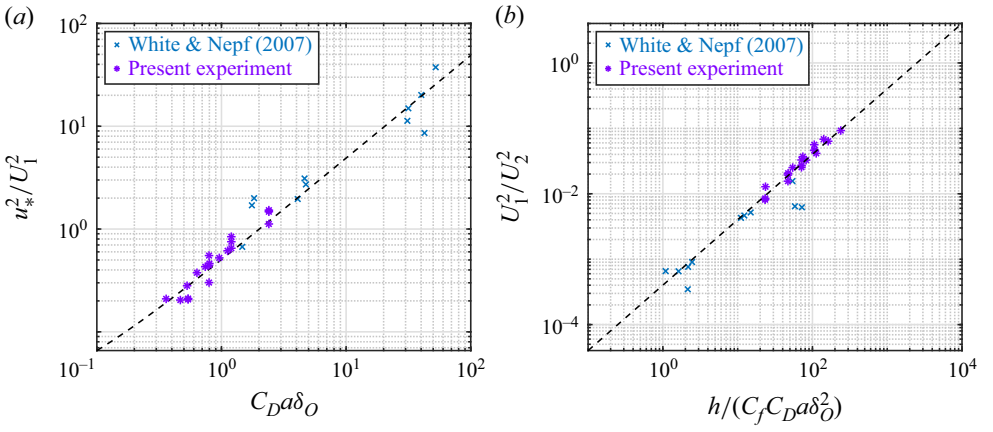

Figure 7. (*a*) The value of u_*^2/U_1^2 scales with $C_D a\delta_O$. The dashed line is the fitted data, $u_*^2/U_1^2 = 0.02 + 0.49 C_D a\delta_O$, with $R^2 = 0.83$. (*b*) The vale of U_1^2/U_2^2 scales with $h/[C_f C_D a\delta_O^2]$. The dashed line is the fitted data, $U_1^2/U_2^2 = 0.0004 h/[C_f C_D a\delta_O^2]$, with $R^2 = 0.92$.

as shown in figure 7(*b*). For unconfined shear layer, $\delta_O \sim h/C_f$, (3.10) becomes

$$\frac{U_1^2}{U_2^2} \sim \frac{C_f}{h}\frac{1}{C_D a}, \tag{3.11}$$

which is consistent with the observations in White & Nepf (2007). This shear-layer scaling applies to both confined and unconfined shear layers, revealing that flow confinement enhances the interior velocity (U_1) and interfacial shear stress ($-\overline{u'v'}$) by improving the pressure gradient.

3.2. *Vortex formation and interaction*

Within the shear layer, the initiation of coherent structures was identified by a distinct peak in the low-frequency region of the cross-power spectral density of the streamwise velocity and spanwise velocity (S_{uv}, as shown in figures 8 and 9). Normalised by the momentum thickness, θ (defined in (1.2)), and advection velocity, U_c, the dominant dimensionless frequency agrees fairly well with the value predicted for KH instability within a free shear layer, $f\theta/U_c = 0.032$ (Ho & Huerre 1984). This agreement suggests that the shear instability can self-organise under varying array densities and blockage ratios, even the growth of shear layer was restricted and flow confinement occurs. At $2b/B < 0.5$, no peak was observed near the channel centreline, reflecting the absence of turbulent structures as the shear layer had not extended to the centreline (figure 9). However, as the array expanded laterally ($2b/B > 0.5$), a distinct peak emerged at the channel centreline (figures 9, 10), indicating the presence of coherent structures, despite the time-averaged shear stress being nearly zero at this position ($-\overline{u'v'} \approx 0$ at $y = 0$). The zero time-averaged shear stress and the presence of a peak in S_{uv} suggest that turbulent interaction occurred and this interaction resulted in a balancing effect between these two shear layers. Due to the symmetrical configuration, the coherent structures initiated at two interfaces possessed equal strength but rotated in opposite directions. Evaluated by the magnitude of the peaks in S_{uv}, the vortex intensity was insensitive to the array density, consistent with the observation from the peak of shear stress (figure 4*b*). However, as the array extended laterally (figure 9), the vortex intensity was highly improved, even though the velocity shear across the interface was mitigated (figure 3*b*). The consistency of the

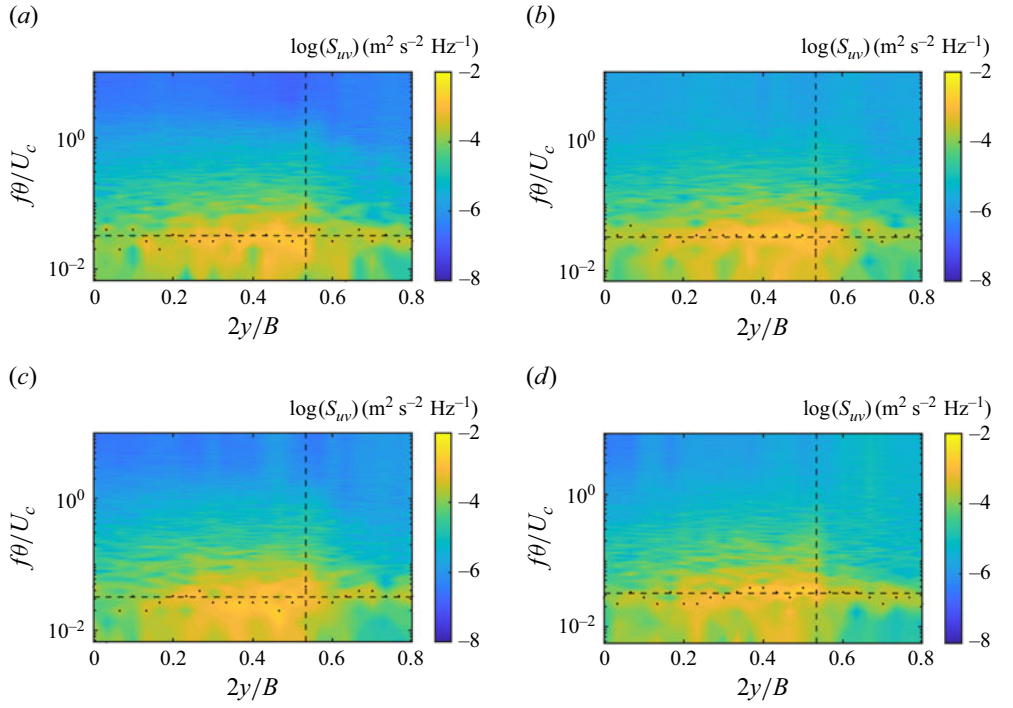

Figure 8. Lateral distributions of cross-power spectral density (S_{uv}) in the fully developed region for $2b/B = 0.47$ under varying array densities: (*a*) $\Phi = 0.9\,\%$; (*b*) $\Phi = 1.3\,\%$; (*c*) $\Phi = 2.0\,\%$; (*d*) $\Phi = 4.0\,\%$. The vertical dashed line marks the lateral interface of the array, while the horizontal dashed line indicates the normalised natural frequency of mixing layers, $f\theta/U_c = 0.032$ (Ho & Huerre 1984). The dots indicate the peak normalised frequencies for each data point collected.

dominant frequencies across the channel width reveals a vortex synchronisation between the two vortex streets.

Figure 10 shows the turbulent interaction at the channel centreline from the perspective of energy. At $2b/B > 0.5$, a -3 slope was observed on the high-frequency side of the peak in S_{uv}, suggesting that the coherent structures formed were quasi-two-dimensional (Proust *et al.* 2017; Truong *et al.* 2019). In the high-frequency region in S_{uv}, the slope improved from almost horizontal (dark blue in figure 10) to $-5/3$ as the blockage ratio increased from $2b/B = 0.33$ to 0.67, indicating the contribution to shear-scale turbulence dissipation was shifted from bed friction to a turbulent viscous effect cause by turbulent interaction (Nezu, Nakagawa & Jirka 1994). Furthermore, this improvement reveals that the turbulent interaction highly accelerated the transformation of large coherent structures into smaller-scale turbulent structures in the open region (Rathod *et al.* 2025). This improved transformation is consistent with the faster mitigation of the shear stress in the open region, indicated by the larger lateral gradient of the shear stress, $-\partial\overline{u'v'}/\partial y$ as shown in figure 5(*b*). In addition, the peak and the corresponding frequency improved as the blockage ratio increased, manifesting the enhanced vortex energy and more rapid vortex shedding. For example, when $2b/B$ increased from 0.53 to 0.67, the dominant frequency rose from 0.15 to 0.2 Hz, indicating that the vortex period decreased from 6.7 to 5.0 s at the centre of the flume. Within the sampling duration (120 s) in the present work, the number of observed vortices increased from 18 to 20, revealing the flow confinement enhanced the vortex shedding at the channel centreline.

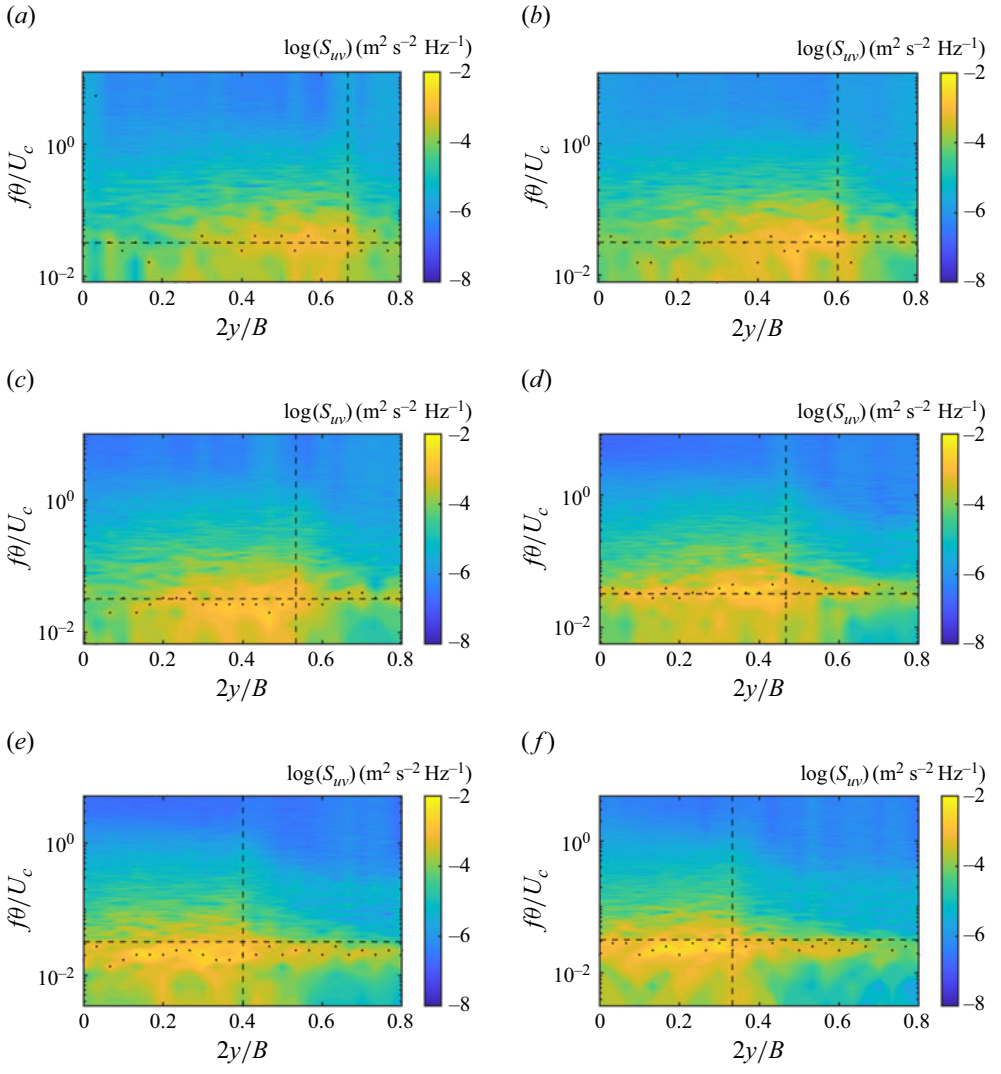

Figure 9. Lateral distributions of cross-power spectral density (S_{uv}) in the fully developed region for $\Phi =$ 2.0 % under varying array blockage ratios: (*a*) $2b/B = 0.33$; (*b*) $2b/B = 0.40$; (*c*) $2b/B = 0.47$; (*d*) $2b/B =$ 0.53; (*e*) $2b/B = 0.60$; (*f*) $2b/B = 0.67$. The vertical dashed line marks the lateral interface of the array, while the horizontal dashed line indicates the normalised natural frequency of mixing layers, $f\theta/U_c = 0.032$ (Ho & Huerre 1984). The dots indicate the peak normalised frequencies for each data point collected.

Furthermore, although the normalised frequency of the vortex agrees fairly well with the normalised natural frequency of the mixing layers predicted by linear stability analysis (Ho & Huerre 1984), the reduction in the width of the open region highly improved the frequency of the coherent structures at the side edges, from 0.06 to 0.19 Hz (figure 11*a*). This is probably due to the reduction in vortex size, which is strongly linked to mixing layer thickness (θ, figure 11*b*), and the increase in advection velocity (U_c, figure 11*c*) (Truong *et al.* 2019). Specially, the reduction in momentum thickness was attributed to the restricted evolution of outer shear layer. These observations comply with previous findings in a single along-bank emergent vegetation canopy (Jia *et al.* 2022), where decreasing the width of the open region led to a smaller wavelength and wave period of the

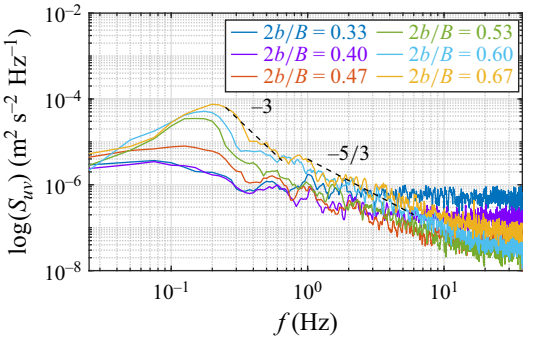

Figure 10. The impact of blockage ratio ($2b/B$) on the cross-power spectral density of the streamwise and spanwise velocity (S_{uv}) for cases with $\Phi = 2.0\,\%$ at the channel centreline ($y = 0$).

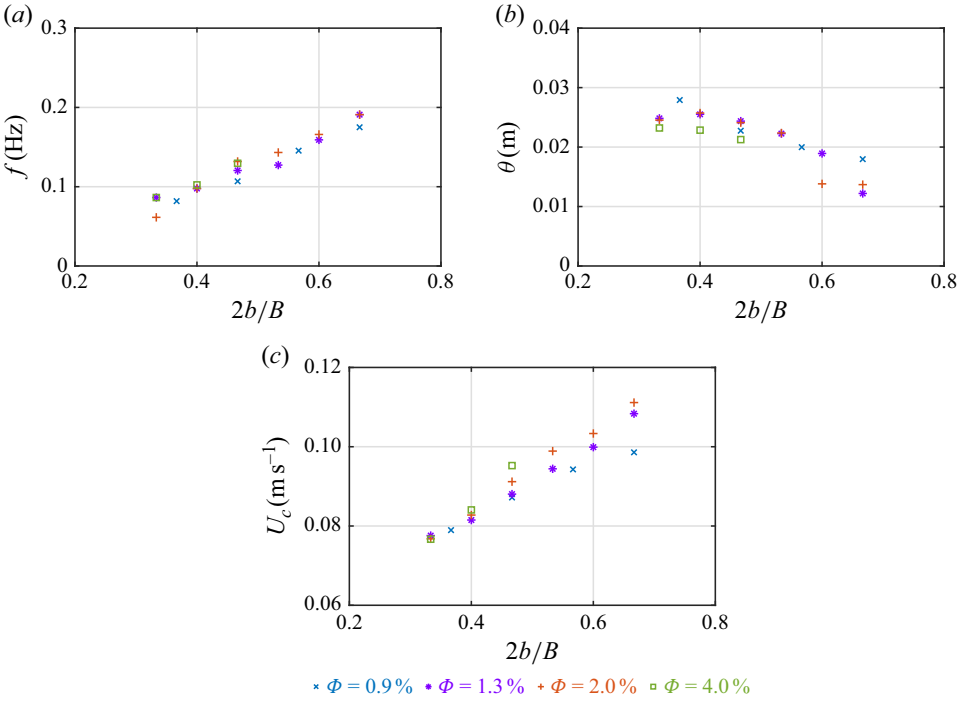

Figure 11. The impact of blockage ratio ($2b/B$) on (a) vortex frequency (f), collected at the array's interface ($y = B/2 - b$), (b) momentum thickness (θ) and (c) advection velocity (U_c).

along-canopy vortices. In their study (Jia *et al.* 2022), the increase in vortex frequency was attributed to the formation of reverse vortices along the sidewall of the open region. In a compound channel with emergent floodplain vegetation, Rathod *et al.* (2025) attributed the enhancement of vortex frequency to the presence of stem-scale vortices, which intensified the dissipation process by breaking down large-scale vortices into smaller horizontal vortices (Zhang & Hu 2023). In addition, the vegetation density presented no distinct influence on vortex frequency and momentum thickness, since the vortex characteristics were mostly dependent on the outer shear layer in the open region (White & Nepf 2007). Overall, the vortex frequency is highly dependent on the vortex size and its correlated dissipation process. Furthermore, the improved frequency means that flow events occur

more rapidly. As a result, sedimentation processes may be significantly influenced in such a way that there is less time for the sediment to be deposited, while the momentum fluxes are larger.

4. Discussion

4.1. *Wave response*

As the array expanded laterally, the dye released from each array was transported over the channel centreline and the interface between the two dye streaks became wavy (figure 12*a*), demonstrating that the turbulent interactions created a wave-like response across the open region. The distinct separation of the dye streaks, rather than mixing, suggests that the vortices became self-organised. Although dye was also present at the channel centreline for $2b/B < 0.5$, no organised behaviour was observed, implying that this phenomenon was attributed to the diffusivity of the dyes rather than vortex evolution (figure 12*b*). For $2b/B > 0.5$, the alternation of the vortex cores from either side of the two arrays in the open region suggests that the vortices organised with a phase shift of π radians (figure 12*b*). Since the centre of each vortex is a low-pressure point that generates a wave response (Zong & Nepf 2011), the alternating vortex cores observed in the present study indicate that low-pressure regions in one array corresponded to high-pressure regions in the other. This vortex alternation intensified the pressure gradient compared with a single interfacial vortex street (Rominger & Nepf 2011). Furthermore, the resulting cross-channel pressure gradient produced a phase shift of $\pi/2$ radians, analogous to the vortex interaction observed across an in-stream finite porous array (Rominger & Nepf 2011). For an in-stream finite porous patch, cross-patch vortex interaction enhanced the vortex intensity strength, as indicated by the enhanced magnitude of the peak shear stress compared with the scenario where vortex interaction was prohibited by placing a splitter plate at the patch centreline (Rominger & Nepf 2011). In contrast to the parallel vortices formed along the streamwise interfaces of an in-stream finite patch, where the left side featured an anti-clockwise rotating vortex and the right side featured a clockwise rotating vortex when facing upstream, the parallel vortices in the present experiments exhibited opposite rotation directions. Specifically, when facing upstream, the vortices on the left side rotated in a clockwise direction, while those developed in the right edge rotated in an anti-clockwise direction (figure 1). Despite the vortex rotation being reversed, the increase in peak shear stress at higher blockage ratios (figure 5*b*) demonstrates that vortex interaction in the open region also contributed to intensifying the vortices by enhancing the cross-stream pressure gradient. Moreover, this interaction improved as the array became more closely spaced. However, the interaction and its corresponding vortex improvement are expected to decay as the array further expands laterally and approaches a channel-spanning patch, which is not considered in the current experiment.

The initiation and interaction of the coherent structures give the velocity time series a strong periodic signature (figure 13, Rominger & Nepf 2011; Li, Liu & Huai 2022). The fluctuating streamwise velocity, $u'(t)$, and fluctuating lateral velocity, $v'(t)$ were perfectly out of phase at the array's interface ($y = B/2 - b$, figure 13*a*), resulting in a phase shift of π radians. These antiphase signals made great contributions to the shear stress, $-\overline{u'v'} > 0$ (figures 4, and 5). Normalised by the vortex period, the normalised phase shift between the horizontal velocity components converged to a value of 0.5 (figure 13*c*), indicating that the vortices were well organised with a phase shift of π radians. Coherence between the streamwise and transverse components at the patch lateral edges existed for all scenarios. In contrast, at the channel centreline ($y = 0$, figure 13*b*), $u'(t)$ and $v'(t)$ were $\pi/2$-radian

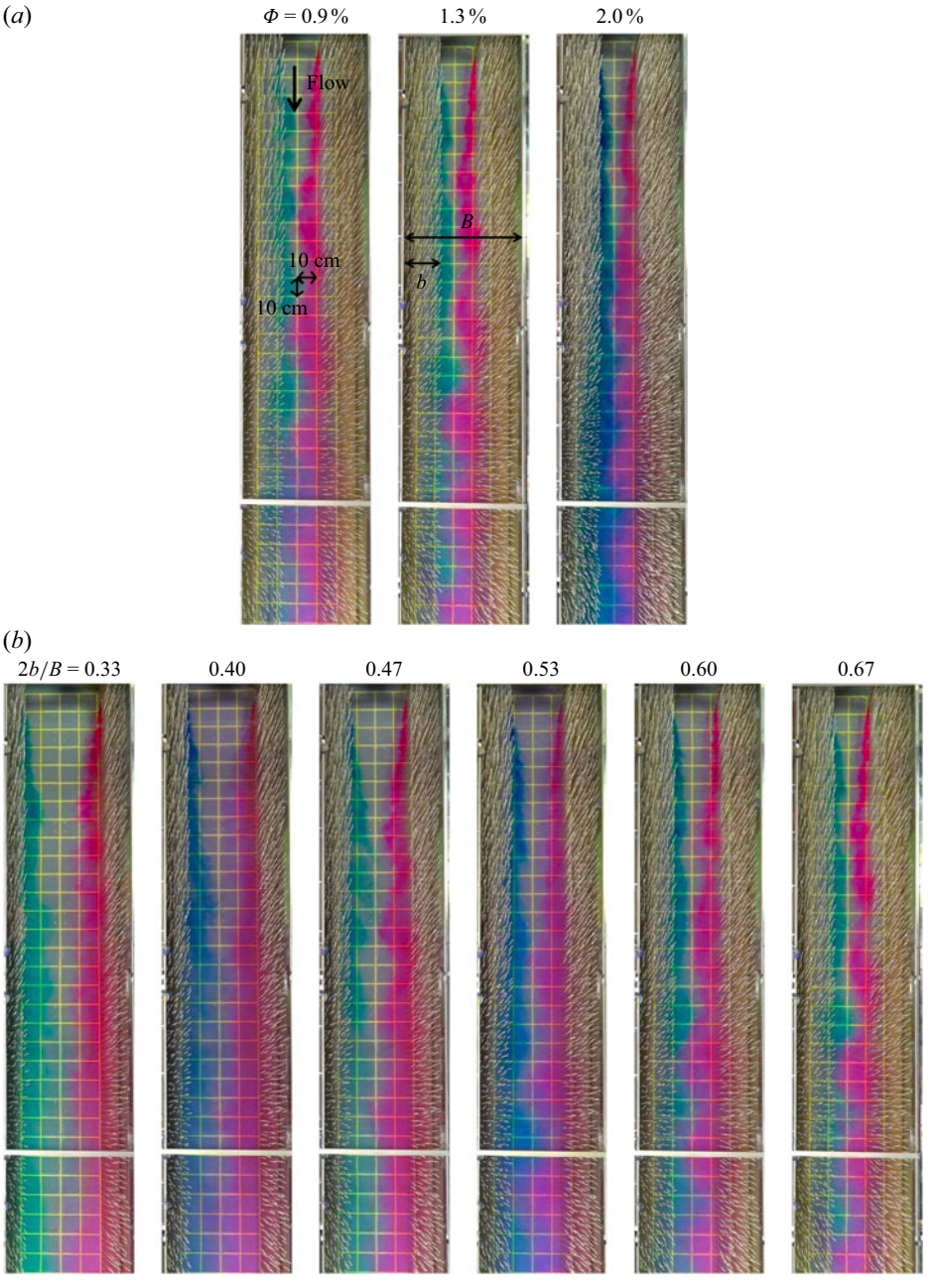

Figure 12. Dye visualisation test. (*a*) The alternation of the vortex cores from each side of the two arrays creates a wave response across the open region, under varying array densities (Φ) for $2b/B = 0.67$. (*b*) The impact of the array-to-channel blockage ratio, $2b/B$, on flow structure in the open region for $\Phi = 1.3\,\%$. The yellow lines mark 10 cm intervals in both the x and y directions. The vertical arrow indicates the flow direction. The horizontal arrows indicate the width of the array, b, and the flume width, B.

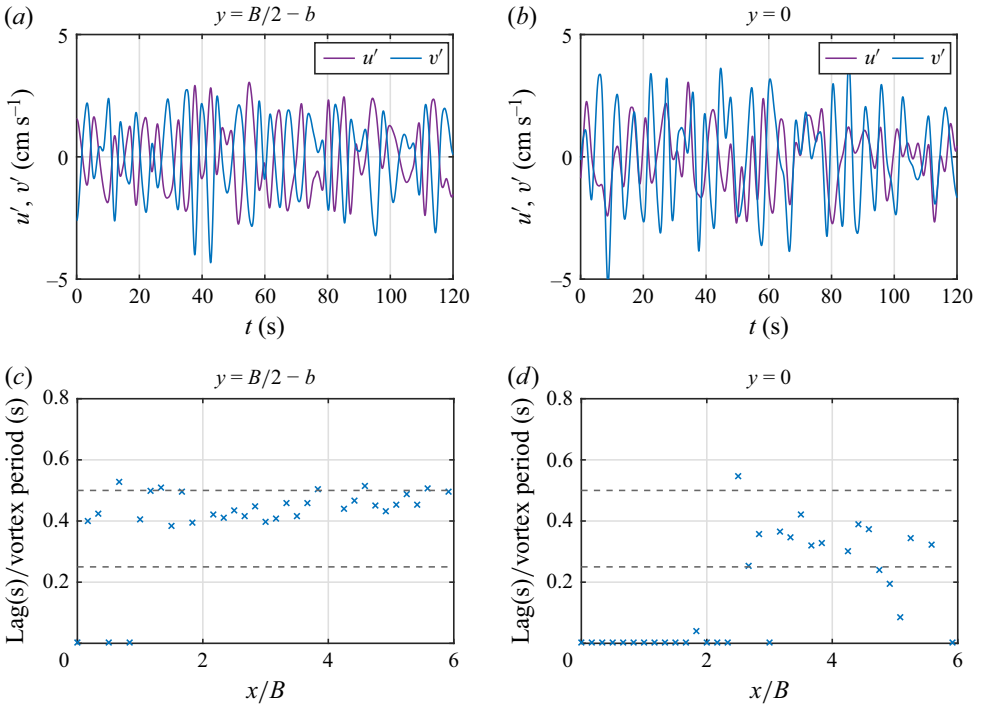

Figure 13. (*a, b*) Time records of fluctuating streamwise velocity, $u'(t)$, and fluctuating transverse velocity, $v'(t)$ and (*c, d*) their corresponding phase shifts at the lateral edge of the array, $y = B/2 - b$, and channel centreline, $y = 0$. The time lags between two signals were normalised by the measured vortex period. The data were collected for case with $\Phi = 0.9\,\%$ and $2b/B = 0.67$. The dashed line of 0.50 suggests a phase shift of π radians. The dashed line of 0.25 indicates a phase shift of $\pi/2$ radians.

out of phase, suggesting that the vortices formed at two the arrays re-organised through wave motion. This is consistent with wavy interface shown in the dye visualisation (figure 12) and previous observations (Zong & Nepf 2011; Rominger & Nepf 2011). The phase shift of $\pi/2$ radians produced no momentum $-\overline{u'v'} = 0$, since the peak of one signal was aligned with the zero crossing of the other signal (figure 13*b*). In this scenario, due to the symmetrically distributed arrays, the shear stress generated from each interface presented the same magnitudes but opposite signs. They balanced each other and produced a zero value at the axis of symmetry, i.e. channel centreline, and the lateral gradient of the shear stress was increased. However, the zero shear stress at $y = 0$ for the unconfined channel was due to the limited penetration of the outer shear ($\delta_O < B/2 - b$). The flow beyond the outer shear was relatively steady, presenting a weak and non-coherent velocity fluctuation.

4.2. *Quadrant analysis*

Quadrant analysis provides information on the contributions of various turbulent events to the turbulent shear stress in the flow (Huai *et al.* 2019). The four quadrants are associated with four different turbulent events, namely outward interactions ($u' > 0,\ v' > 0$), ejections ($u' < 0,\ v' > 0$), inward interactions ($u' < 0,\ v' < 0$) and sweeps ($u' > 0,\ v' < 0$). To associate the flow events with the large-scale coherent structure, the time records of the velocity were filtered with a low frequency, $f = 0.6$ Hz. The filtered low-frequency signals were plotted in the quadrants along with the original measured signals (figure 14). The

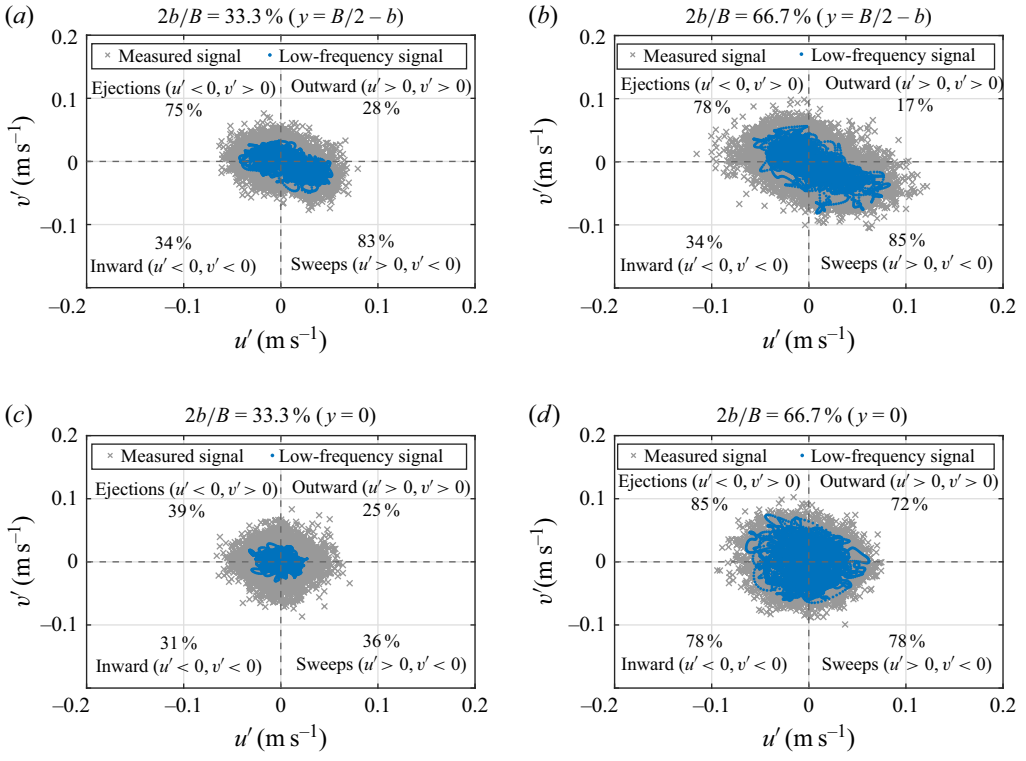

Figure 14. The contribution of large-scale coherent structures to each flow event. The data were collected (*a, b*) at the lateral interface of the array and (*c, d*) channel centreline in the fully developed region, before ($2b/B = 0.33$) and after ($2b/B = 0.67$) the shear layer penetrates to the centreline. The percentage at each quadrant indicates the contribution from the corresponding event.

contribution of each event was accounted separately, because the total shear stress was zero at the channel centreline. Figures 14(*a*) and 14(*b*) show that ejections and sweeps dominated the momentum exchange at the streamwise interfaces of the vegetated zone, in line with the observations in partially vegetated channels (White & Nepf 2008) and compound channels (Truong *et al.* 2019). For confined shear layers, these events became more pronounced, leading to an improved shear stress near the lateral interface of the array (figure 5*b*). However, the contribution of flow events associated with large-scale coherent structures (low-frequency signals) varied from the array edge to the channel centreline. In the channel centreline, the contribution of large-scale coherent structures diminished when the shear layers did not extend to the channel centreline (figure 14*c*), indicating a small influence of large-scale coherent structure at the position. All events intensified as the array widened (figure 14*d*). In this scenario, the presence of these turbulent events at the channel centreline was clearly visualised by dye (figure 12*a*). Specially, ejections and sweeps from one array extended across the centreline towards the opposite array, resulting in a wavy interface between the two dyes. Due to the symmetrical configuration of the system, the contribution of ejections and sweeps from one array can be considered as inward interactions and outward interactions from the other array, respectively. The contributions of outward and inward interactions to shear stress are positive ($u'v' > 0$), whereas those of sweeps and ejections are negative ($u'v' < 0$). The distance from the channel centreline to each array was the same ($B/2 - b$), leading to an equal contribution

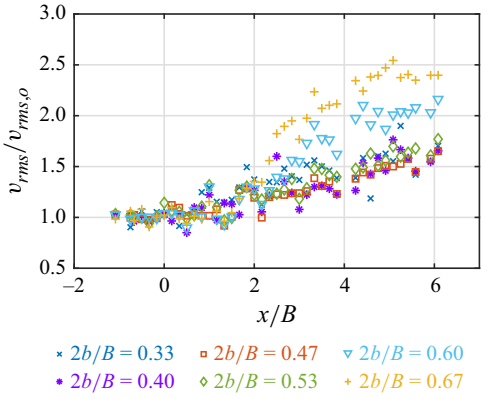

Figure 15. The enhancement of fluctuating lateral velocity (v_{rms}) at the channel centreline under varying blockage ratios ($2b/B$), normalised by upstream fluctuating lateral velocity, $v_{rms,o}$.

of four turbulent events and a zero net shear stress ($\overline{u'v'} = 0$). Furthermore, even though the shear layer did not extend to the channel centreline ($2b/B < 0.5$), the velocity fluctuation (v_{rms}) was improved as the flow developed downstream, and was around 50 % higher than the upstream value (figure 15), attributed to the enhanced flow intensity in the open region. The flow fluctuation was more pronounced when the shear layers were confined ($2b/B > 0.5$), with higher v_{rms} values observed at larger $2b/B$. According to the contribution rate, the improvement in flow fluctuations in the region beyond the shear layer was not dominated by low-frequency structures. As the shear layers reached the centreline, all four events made significant contributions (figure 14*d*), indicating that the momentum exchange shifted from 'jet dominated' to 'shear dominated'. The intensified flow fluctuations and turbulent events suggest that momentum exchange occurred across the channel centreline.

4.3. *Momentum transport*

Compared with a single vortex street, the momentum transport in the open region with turbulent interaction is more complicated. On one hand, the phase shift induced by vortex organisation between the two parallel vortex streets in the open region enhanced the cross-channel pressure gradient, thereby improving flow fluctuations. On the other hand, the vortex frequency was increased, which means that the resident time for the momentum transport was reduced. Considering the improved momentum fluxes and diminished resident time, we applied the wave excursion length (Nepf 2012; Luhar & Nepf 2016), $\Lambda = \sqrt{2}v_{rms}/2\pi f$, to estimate the lateral transport distance from the array's interface. The frequency of the wave motion was consistent with the passing vortices (Zong & Nepf 2011), as indicated by the consistent frequency in S_{uv} across the channel in figure 9, and the fluctuating lateral velocity at the lateral interface was used. Figure 16(*a*) shows that the excursion decayed from $\Lambda = 0.8b$ to $0.2b$, as the blockage ratio increased from 0.33 to 0.67. Although the vortex interaction in the open region highly improved the flow fluctuations, the enhanced frequency and resulting reduced excursion length suggest that the lateral transport was restricted. Thus, for one vortex street, the presence of an opposite vortex street restricted the lateral momentum transport. In contrast, for a finite vegetation patch (Rominger & Nepf 2011), the vortex interaction across the patch produced a wave excursion length over the half-width of the patch, leading to an enhancement of lateral transport.

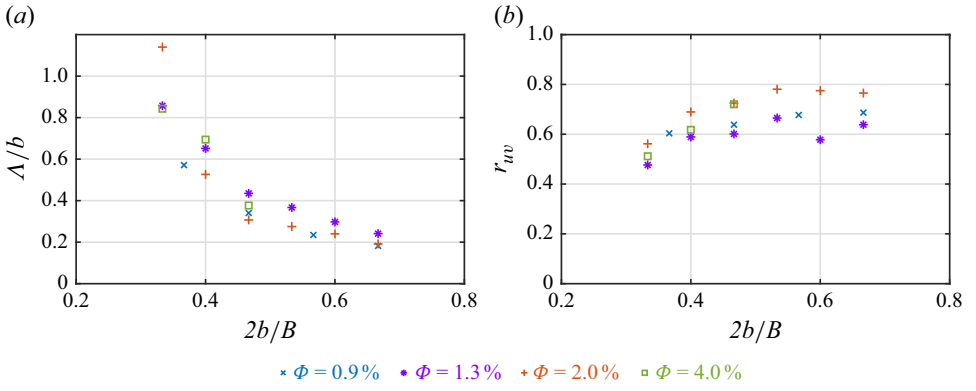

Figure 16. The influence of blockage ratio on the momentum exchange across the array's interface, evaluated by (*a*) wave excursion length, Λ, normalised by the array width, b; and (*b*) Pearson correlation coefficient, r_{uv}.

To evaluate the efficiency of horizontal momentum transport across the array's interface, the Pearson correlation coefficient,

$$r_{uv} = \frac{u_*^2}{u_{rms} v_{rms}}, \tag{4.1}$$

was considered. Figure 16(*b*) observes that the array expansion improved the efficiency of momentum transport across the patch interface before the shear layers were confined ($2b/B < 0.5$), presenting $r_{uv} \approx 0.5 \sim 0.7$. In this scenario, the increased efficiency of momentum transport was associated with enhanced vortex strength. However, when the two shear layers met and interacted at the channel centreline ($2b/B > 0.5$), r_{uv} approached a constant value of approximately 0.7, even as the vortices continued to intensify. This constant r_{uv} further indicates that the shear layer formed at one array acted like an additional resistance to the shear layer developed at the other array in a vegetation–channel–vegetation system, thereby limiting the momentum transport. In boundary layer flows and canonical mixing layers, typical values of r_{uv} were ≈ 0.32 and ≈ 0.44, respectively (Ghisalberti & Nepf 2002). For partially obstructed channels with emergent complex foliated plants and leafless plants, r_{uv} values were ≈ 0.6 and ≈ 0.4, respectively (Caroppi *et al.* 2019). Compared with the r_{uv} value observed for a single vortex street, the $r_{uv} \approx 0.7$ value at $2b/B > 0.5$ in the present experiment indicates that the shear-layer-induced confinement highly intensified the shear-layer vortices, thereby enhancing the efficiency of momentum transport across the lateral edges of the array. However, the significant turbulent interactions limit further enhancement by introducing mutual resistance among the shear instabilities.

This vegetation–channel–vegetation system generated a lateral flow pattern characterised by a slow–fast–slow velocity distribution, which is the reverse of the fast–slow–fast pattern observed in an in-stream finite vegetation patch. For an in-stream finite vegetation patch with two flow-parallel interfaces separated by the low-speed interior velocity, the vortex interaction across the patch width transported the momentum from the high-discharge side regions towards the low-discharge vegetated region, thereby mitigating the velocity deficit (Rominger & Nepf 2011). This was referred to the formation of a von Kármán-like vortex (Zhang *et al.* 2023). The diminished velocity shear in turn weakened the coherent structures as they developed downstream (Zhang *et al.* 2024). However, the vortices in the present experiment interacted across a high-speed open

region, behaving like a reverse von Kármán vortex street (Xu, Duan & Xu 2017). The high-speed flow in the central region performed like a jet flow, imposing a 'diverting' effect toward the adjacent vegetated regions. Concurrently, the plant-induced resistance exerted a constraining impact on this outward diversion, contributing to sustaining the vortex alterations in the open region. Overall, the spatial structure of the reverse von Kármán vortex street is self-sustained under the confined condition while the regular von Kármán vortex street is not stable.

5. Conclusion

In this paper, we conducted a laboratory experiment to investigate the flow adjustment, shear-layer growth and turbulent interaction within a symmetrical vegetation–channel–vegetation system. A total of 19 configurations of varying patch densities and widths (b) were considered for investigation, with the aid of rigorous velocity measurements and dye visualisations.

In the present symmetrical configuration, shear layers initiated at both lateral interfaces of the vegetation array simultaneously grow in the open region. Scaling analysis suggests that, in the outer shear layer, shear stress is primarily balanced by the pressure gradient. When the outer shear layer was fully developed before reaching the channel centreline, the pressure gradient is balanced by bed friction, so that the flow adjustment and shear structure were largely insensitive to the array-to-channel blockage ratio. In this scenario, the fully developed outer penetration length is given by $\delta_O \sim h/C_f$, where h is the water depth and C_f is the bed friction coefficient. With the constant water depth and bed friction considered in this study, a constant outer thickness of $\delta_O = 0.5(B/2)$ was observed, where B is the width of the channel, when each array width $b < 0.5(B/2)$, corresponding to a blockage ratio of $2b/B < 0.5$. As the array extended laterally ($2b/B > 0.5$), flow confinement appears when the outer shear layers penetrate to the channel centreline. The thickness of each outer penetration was then restricted to the half-width of the open region, $\delta_O = B/2 - b$. In this regime, flow confinement amplifies the pressure gradient, producing a higher interior velocity within the vegetated region and an intensified turbulent structure along the edge, relative to the fully developed shear layer observed in the present experiment and previous studies. In general, the flow confinement presents when the full penetration thickness of the outer shear layer is larger than the half-width of the open region. However, if water depth or bed friction coefficient varies, the threshold value for flow confinement might change because the full penetration of the outer layer is altered.

Furthermore, within the shear layer, coherent structures were triggered through KH instability, with a normalised frequency agrees fairly well with the normalised natural frequency of the mixing layers. Although the shear-layer vortices can self-organise even under confined conditions, increasing the blockage ratio from 0.33 to 0.67 led to an increase in vortex frequency by over 100 %, a reduction in momentum thickness by approximately 60 %, and an increase in convection velocity by approximately 40 %. The time-averaged shear stress was zero at the centreline when the shear layer was confined to one half of the open region, but the shear-layer vortices interacted across the open region, yielding significant but equally contributing turbulent events from both sides. Furthermore, a wavy interface was visualised by dyes released at two side edges, revealing a wave motion with a phase shift of π radians between the parallel vortex streets. The alternating low-pressure vortex cores between the parallel vortex streets amplify the pressure gradient, intensifying coherent structures and facilitating momentum exchange across the channel centreline. While the turbulent intensity improves, the decrease in

residence time for the turbulent flow events may lead to shorter transport distances, from $0.8b$ to $0.2b$. Consequently, the shear layer developed on one interface acts as an extra resistance to shear turbulence on the opposite interface. From the perspective of vegetation restoration and management in natural channels or urban drainage systems, the width of the vegetation array should be carefully considered to minimise the flow confinement effect. Intense flow confinement can enhance the velocity within vegetated zones and elevate turbulence at the patch edges, which may reduce sediment retention within the patch and promote erosion along the patch boundaries.

To make our conclusions more applicable to different scenarios, further investigation into the characteristics of the array is necessary, as factors such as stem size, stem alignment, flexibility, degree of submergence and surface area (skin friction) can significantly influence patch hydraulic resistance, velocity shear and vortex structure. Additionally, a wider range of hydraulic conditions should be considered, since variables like water depth and bed friction coefficient can also impact the development of shear layers in open region.

Funding. This research was supported by the Hong Kong Research Grants Council (RGC) under Project No. C5002-22Y and NSFC/RGC Joint Research Scheme under Project. No. N_PolyU559/22.

Declaration of interests. The authors report no conflict of interest.

References

BALKE, T., KLAASSEN, P.C., GARBUTT, A., VAN DER WAL, D., HERMAN, P.M.J. & BOUMA, T.J. 2012 Conditional outcome of ecosystem engineering: a case study on tussocks of the salt marsh pioneer Spartina anglica. *Geomorphology* **153–154**, 232–238.

BEN MEFTAH, M. & MOSSA, M. 2016 Partially obstructed channel: contraction ratio effect on the flow hydrodynamic structure and prediction of the transversal mean velocity profile. *J. Hydrol.* **542**, 87–100.

BOUMA, T.J., VAN DUREN, L.A., TEMMERMAN, S., CLAVERIE, T., BLANCO-GARCIA, A., YSEBAERT, T. & HERMAN, P.M.J. 2007 Spatial flow and sedimentation patterns within patches of epibenthic structures: combining field, flume and modelling experiments. *Cont. Shelf Res.* **27** (8), 1020–1045.

BROWN, G.L. & ROSHKO, A. 1974 On density effects and large structure in turbulent mixing layers. *J. Fluid Mech.* **64** (4), 775–816.

CAROPPI, G., GUALTIERI, P., FONTANA, N. & GIUGNI, M. 2020 Effects of vegetation density on shear layer in partly vegetated channels. *J. Hydro-environ. Res.* **30**, 82–90.

CAROPPI, G., VÄSTILÄ, K., GUALTIERI, P., JÄRVELÄ, J., GIUGNI, M. & ROWIŃSKI, P.M. 2021 Comparison of flexible and rigid vegetation induced shear layers in partly vegetated channels. *Water Resour. Res.* **57** (3), e2020WR028243.

CAROPPI, G., VÄSTILÄ, K., JÄRVELÄ, J., ROWIŃSKI, P.M. & GIUGNI, M. 2019 Turbulence at water-vegetation interface in open channel flow: experiments with natural-like plants. *Adv. Water Resour.* **127**, 180–191.

CHEN, Z., JIANG, C. & NEPF, H. 2013 Flow adjustment at the leading edge of a submerged aquatic canopy. *Water Resour. Res.* **49** (9), 5537–5551.

DUPUIS, V., PROUST, S., BERNI, C. & PAQUIER, A. 2017 Mixing layer development in compound channel flows with submerged and emergent rigid vegetation over the floodplains. *Exp. Fluids* **58** (4), 30.

FRANKLIN, P., DUNBAR, M. & WHITEHEAD, P. 2008 Flow controls on lowland river macrophytes: a review. *Sci. Total Environ.* **400** (1), 369–378.

GHISALBERTI, M. & NEPF, H. 2006 The structure of the shear layer in flows over rigid and flexible canopies. *Environ. Fluid Mech.* **6**, 277–301.

GHISALBERTI, M. & NEPF, H.M. 2002 Mixing layers and coherent structures in vegetated aquatic flows. *J. Geophys. Res.: Oceans* **107** (C2), 3–1–3–11.

GHISALBERTI, M. & NEPF, H.M. 2004 The limited growth of vegetated shear layers. *Water Resour. Res.* **40** (7), W07502.

GHISALBERTI, M. & NEPF, H.M. 2009 Shallow flows over a permeable medium: the hydrodynamics of submerged aquatic canopies. *Transport Porous Med.* **78** (2), 309–326.

GORING, D.G. & NIKORA, V.I. 2002 Despiking acoustic doppler velocimeter data. *J. Hydraul. Engng* **128** (1), 117–126.

GURNELL, A.M. & GRABOWSKI, R.C. 2016 Vegetation–hydrogeomorphology interactions in a low-energy, human-impacted river. *River Res. Appl.* **32** (2), 202–215.
HO, C.M. & HUERRE, P. 1984 Perturbed free shear layers. *Annu. Rev. Fluid Mech.* **16**, 365–424.
HOSSEINI, N., GRIFFITH, M.D. & LEONTINI, J.S. 2020 The flow past large numbers of cylinders in tandem. *J. Fluid. Struct.* **98**, 103103.
HUAI, W., XUE, W. & QIAN, Z. 2015 Large-eddy simulation of turbulent rectangular open-channel flow with an emergent rigid vegetation patch. *Adv. Water Resour.* **80**, 30–42.
HUAI, W.-X., ZHANG, J., WANG, W.-J. & KATUL, G.G. 2019 Turbulence structure in open channel flow with partially covered artificial emergent vegetation. *J. Hydrol.* **573**, 180–193.
JIA, Y.-Y., YAO, Z.-D., DUAN, H.-F., WANG, X.-K.W. & YAN, X-F. 2022 Numerical assessment of canopy blocking effect on partly-obstructed channel flows: from perturbations to vortices. *Engng Appl. Comput. Fluid* **16** (1), 1761–1780.
KIM, H.S., KIMURA, I. & SHIMIZU, Y. 2015 Bed morphological changes around a finite patch of vegetation. *Earth Surf. Process. Land.* **40** (3), 375–388.
KOKEN, M. & CONSTANTINESCU, G. 2023 Influence of submergence ratio on flow and drag forces generated by a long rectangular array of rigid cylinders at the sidewall of an open channel. *J. Fluid Mech.* **966**, A5.
LEI, J. & NEPF, H. 2021 Evolution of flow velocity from the leading edge of 2-D and 3-D submerged canopies. *J. Fluid Mech.* **916**, A36.
LI, D., LIU, M. & HUAI, W. 2022 Modeling transverse momentum exchange in partially vegetated flow. *Phys. Fluids* **34** (2), 025124.
LIU, C. & NEPF, H. 2016 Sediment deposition within and around a finite patch of model vegetation over a range of channel velocity. *Water Resour. Res.* **52** (1), 600–612.
LIU, D., DIPLAS, P., FAIRBANKS, J.D. & HODGES, C.C. 2008 An experimental study of flow through rigid vegetation. *J. Geophys. Res.: Earth Surface* **113** (F4), F04015.
LUHAR, M. & NEPF, H.M. 2016 Wave-induced dynamics of flexible blades. *J. Fluid. Struct.* **61**, 20–41.
LUHAR, M., ROMINGER, J. & NEPF, H. 2008 Interaction between flow, transport and vegetation spatial structure. *Environ. Fluid Mech.* **8**, 423–439.
MORRIS, E.P., PERALTA, G., BRUN, F.G., VAN DUREN, L., BOUMA, T.J. & PEREZ-LLORENS, J.L. 2008 Interaction between hydrodynamics and seagrass canopy structure: spatially explicit effects on ammonium uptake rates. *Limnol. Oceanogr.* **53** (4), 1531–1539.
MULAHASAN, S., STOESSER, T. & MCSHERRY, R. 2017 Effect of floodplain obstructions on the discharge conveyance capacity of compound channels. *J. Irrig. Drain. Engng* **143** (11), 04017045.
NEPF, H.M. 2012 Hydrodynamics of vegetated channels. *J. Hydraul. Res.* **50** (3), 262–279.
NEPF, H., GHISALBERTI, M., WHITE, B. & MURPHY, E. 2007 Retention time and dispersion associated with submerged aquatic canopies. *Water Resour. Res.* **43** (4), W04422.
NEPF, H.M. & VIVONI, E.R. 2000 Flow structure in depth-limited, vegetated flow. *J. Geophys. Res.: Oceans* **105** (C12), 28547–28557.
NEZU, I., NAKAGAWA, H. & JIRKA, G.H. 1994 Turbulence in open channel flows. *J. Hydraul. Engng* **120** (10), 1235–1237.
NEZU, I. & SANJOU, M. 2008 Turburence structure and coherent motion in vegetated canopy open-channel flows. *J. Hydro-environ. Res.* **2** (2), 62–90.
OKAMOTO, T.-A. & NEZU, I. 2013 Spatial evolution of coherent motions in finite-length vegetation patch flow. *Environ. Fluid Mech.* **13** (5), 417–434.
PELTIER, Y. 2011 Physical modelling of overbank flows with a groyne set on the floodplain. PhD thesis, Université Claude Bernard-Lyon I.
PROUST, S., FERNANDES, J.N., LEAL, J.B., RIVIÈRE, N. & PELTIER, Y. 2017 Mixing layer and coherent structures in compound channel flows: effects of transverse flow, velocity ratio, and vertical confinement. *Water Resour. Res.* **53** (4), 3387–3406.
PROUST, S., FERNANDES, J.N., PELTIER, Y., LEAL, J.B., RIVIERE, N. & CARDOSO, A.H. 2013 Turbulent non-uniform flows in straight compound open-channels. *J. Hydraul. Res.* **51** (6), 656–667.
RATHOD, L.V., TIMBADIYA, P.V. & BARMAN, B. 2025 Turbulent anisotropy and coherent structures in flow through a symmetric compound channel with emergent floodplain vegetation. *Phys. Fluids* **37** (1), 015174.
ROMINGER, J.T. & NEPF, H.M. 2011 Flow adjustment and interior flow associated with a rectangular porous obstruction. *J. Fluid Mech.* **680**, 636–659.
SAHIN, M. & OWENS, R.G. 2004 A numerical investigation of wall effects up to high blockage ratios on two-dimensional flow past a confined circular cylinder. *Phys. Fluids* **16** (5), 1305–1320.
SONG, S.-Y., WANG, X.-K., DUAN, H.-F., STOCCHINO, A. & YAN, X.-F. 2024 Numerical investigation of a three-dimensional flow structure influenced by the lateral expansion of a partially distributed submerged canopy. *Phys. Fluids* **36** (8), 085164.

STOCCHINO, A., BESIO, G., ANGIOLANI, S. & BROCCHINI, M. 2011 Lagrangian mixing in straight compound channels. *J. Fluid Mech.* **675**, 168–198.

STOCCHINO, A. & BROCCHINI, M. 2010 Horizontal mixing of quasi-uniform straight compound channel flows. *J. Fluid Mech.* **643**, 425–435.

SUKHODOLOV, A.N. & SUKHODOLOVA, T.A. 2010 Case study: effect of submerged aquatic plants on turbulence structure in a lowland river. *J. Hydraul. Engng* **136** (7), 434–446.

TRUONG, S.H., UIJTTEWAAL, W.S.J. & STIVE, M.J.F. 2019 Exchange processes induced by large horizontal coherent structures in floodplain vegetated channels. *Water Resour. Res.* **55** (3), 2014–2032.

WANG, X., CHEN, J., ZHOU, B., LI, Y. & XIANG, Q. 2021 Experimental investigation of flow past a confined bluff body: Effects of body shape, blockage ratio and Reynolds number. *Ocean Engng* **220**, 108412.

WANG, Z.-R., ZHANG, S.-J., JIANG, Y.-X., YAO, Z.-D. & XU-FENG, Y. 2024 Evaluating shallow mixing layer in partially-distributed canopy flows using da-les: bed friction, water shallowness and canopy denseness. *Engng Appl. Comput. Fluid* **18** (1), 2298075.

WELCH, P. 1967 The use of fast Fourier transform for the estimation of power spectra: a method based on time averaging over short, modified periodograms. *IEEE Trans. Audio Electroacoust.* **15** (2), 70–73.

WHITE, B.L. & NEPF, H.M. 2007 Shear instability and coherent structures in shallow flow adjacent to a porous layer. *J. Fluid Mech.* **593**, 1–32.

WHITE, B.L. & NEPF, H.M. 2008 A vortex-based model of velocity and shear stress in a partially vegetated shallow channel. *Water Resour. Res.* **44** (1), W01412.

WHITE, F.M. & MAJDALANI, J. 2006 Viscous fluid flow, vol. 3, : McGraw-Hill New York.

WILSON, C.A.M.E., STOESSER, T., BATES, P.D. & PINZEN, A.B. 2003 Open channel flow through different forms of submerged flexible vegetation. *J. Hydraul. Engng* **129** (11), 847–853.

XU, G.D., DUAN, W.Y. & XU, W.H. 2017 The propulsion of two flapping foils with tandem configuration and vortex interactions. *Phys. Fluids* **29** (9), 097102.

YAN, X.F., DUAN, H.F., WAI, W.H.O., LI, C.W. & WANG, X.K. 2022 Spatial flow pattern, multi-dimensional vortices, and junction momentum exchange in a partially covered submerged canopy flume. *Water Resour. Res.* **58** (3), e2020WR029494.

ZHANG, J. & HU, R. 2023 Turbulence structure in an experimental compound channel with varying coverage of riparian vegetation on the floodplain. *J. Hydrol.* **620**, 129378.

ZHANG, J., LEI, J., HUAI, W. & NEPF, H. 2020 Turbulence and particle deposition under steady flow along a submerged seagrass meadow. *J. Geophys. Res.: Oceans* **125** (5), e2019JC015985.

ZHANG, Y.-H., DUAN, H.-F., YAN, X.-F. & STOCCHINO, A. 2023 Experimental study on the combined effects of patch density and elongation on wake structure behind a rectangular porous patch. *J. Fluid Mech.* **959**, A36.

ZHANG, Y.-H., DUAN, H.-F., YAN, X.-F. & STOCCHINO, A. 2024 Quantifying wake dynamics subjected to stream vegetation patch elongation: the influence of patch-edge vortices. *Phys. Fluids* **36** (5), 055108.

ZHAO, T. & NEPF, H.M. 2021 Turbulence dictates bedload transport in vegetated channels without dependence on stem diameter and arrangement. *Geophys. Res. Lett.* **48** (21), e2021GL095316.

ZONG, L. & NEPF, H. 2010 Flow and deposition in and around a finite patch of vegetation. *Geomorphology* **116** (3), 363–372.

ZONG, L. & NEPF, H. 2011 Spatial distribution of deposition within a patch of vegetation. *Water Resour. Res.* **47** (3), W03516.

ZONG, L. & NEPF, H. 2012 Vortex development behind a finite porous obstruction in a channel. *J. Fluid Mech.* **691**, 368–391.